nature materials

ARTICLES

https://doi.org/10.1038/s41563-017-0006-0

Thermochromic halide perovskite solar cells

Jia Lin[1,2,3], Minliang Lai[1], Letian Dou[1,2,4], Christopher S. Kley[1], Hong Chen[1], Fei Peng[5], Junliang Sun[5], Dylan Lu[1,2], Steven A. Hawks[1,2,6], Chenlu Xie[1], Fan Cui[1], A. Paul Alivisatos[1,2,7,8], David T. Limmer[1,2,7] and Peidong Yang[1,2,7,8]*

Smart photovoltaic windows represent a promising green technology featuring tunable transparency and electrical power generation under external stimuli to control the light transmission and manage the solar energy. Here, we demonstrate a thermochromic solar cell for smart photovoltaic window applications utilizing the structural phase transitions in inorganic halide perovskite caesium lead iodide/bromide. The solar cells undergo thermally-driven, moisture-mediated reversible transitions between a transparent non-perovskite phase (81.7% visible transparency) with low power output and a deeply coloured perovskite phase (35.4% visible transparency) with high power output. The inorganic perovskites exhibit tunable colours and transparencies, a peak device efficiency above 7%, and a phase transition temperature as low as 105 °C. We demonstrate excellent device stability over repeated phase transition cycles without colour fade or performance degradation. The photovoltaic windows showing both photoactivity and thermochromic features represent key stepping-stones for integration with buildings, automobiles, information displays, and potentially many other technologies.

Smart windows with reversible and persistent colour changes to modulate visible light transmittance have been reported using electrochromic, thermochromic, and liquid crystal materials[1–3]. The transparency of such windows is controlled simply by absorbing or reflecting sunlight without actually converting the solar energy into a useful form. To date, semi-transparent photovoltaics have been demonstrated for power-generating windows that provide shading, lighting, and power output[4,5], but without any colour-changing characteristics. Photovoltaic windows with switchable transparencies—smart photovoltaic windows—which can harvest and manage the incoming solar energy have been developed only by combining semi-transparent solar cells with additional chromic components to form multi-junction tandem devices[6–8]. It is highly desirable to develop a stable and photoactive material possessing two intrinsic states that have large colour contrast, one with high transparency to ensure the greatest brightness, and the other with strong light absorption to produce sufficient electrical energy, where the two states can be reversibly switched back and forth in response to the external environment. Materials with structural phase transitions have been found inherently linked to substantially different optical, electronic, and/or thermal properties due to distinct atomic arrangements of each specific crystal structure[9,10]. In particular, non-volatile and fully-reversible phase transitions suggest the possibility of applications in smart photovoltaic windows. The concept has not been realized because most of the semiconductors cannot be switched between a transparent phase and a non-transparent phase reversibly, without deteriorating their electronic properties.

Recently, halide perovskites of an ABX_3 structure [$A = CH_3NH_3^+$ (MA), $HC(NH_2)_2^+$ (FA), Cs^+; $B = Pb^{2+}$, Sn^{2+}; $X = I^-$, Br^-, Cl^-] have emerged as intriguing photovoltaic materials and become a rapidly evolving field[11,12]. The prototypical organic–inorganic hybrid perovskite methylammonium lead iodide ($MAPbI_3$) was reported to undergo multiple temperature-dependent phase transitions, with a change from the tetragonal to the cubic phase at ~60 °C, within the solar cell operating temperature range[13,14]. However, the structural properties vary only little between the two phases, with slight tilting of the three-dimensional metal-halide octahedral network. Consequently, both the optoelectronic properties and solar cell performances do not alter significantly upon phase transition. Another promising halide perovskite material is the purely inorganic version, caesium lead iodide/bromide ($CsPbI_{3-x}Br_x$, $0 \le x \le 3$). These inorganic perovskites have achieved significantly enhanced thermal and environmental stability, and are considered to be potentially on a par with the organic–inorganic hybrid species in terms of intrinsic solar cell performance ability[15,16]. Substantial structural changes occur in these inorganic perovskites upon phase transitions, often between a room-temperature non-perovskite phase (low-T phase) and a high-temperature perovskite phase (high-T phase)[17,18]. These two phases feature distinct optoelectronic properties such as the bandgap, photoluminescence (PL) quantum efficiency, and charge carrier mobility and lifetime[14,15]. Here we examine the structural phase transition behaviours in such inorganic mixed halide perovskite $CsPbI_{3-x}Br_x$ thin films. The large structural changes induced by phase transitions lead to films with two switchable characteristic states with distinct visible transparencies and photovoltaic device efficiencies, making them promising candidates for smart photovoltaic windows.

Figure 1a schematically illustrates the crystal structure change between the low-T and high-T phases of $CsPbI_{3-x}Br_x$. The low-T to high-T phase transition occurs upon reaching the transition temperature by thermal heating (in inert or ambient condition) with the high-T phase being kinetically trapped and metastable in an inert environment when cooled to room temperature. Critical to

[1]Department of Chemistry, University of California, Berkeley, California, USA. [2]Materials Sciences Division, Lawrence Berkeley National Laboratory, Berkeley, California, USA. [3]Department of Physics, Shanghai University of Electric Power, Shanghai, China. [4]Davidson School of Chemical Engineering, Purdue University, West Lafayette, Indiana, USA. [5]Berzelii Center EXSELENT on Porous Materials, Department of Materials and Environmental Chemistry, Stockholm University, Stockholm, Sweden. [6]Lawrence Livermore National Laboratory, Livermore, California, USA. [7]Kavli Energy NanoScience Institute, Berkeley, California, USA. [8]Department of Materials Science and Engineering, University of California, Berkeley, California, USA. Jia Lin, Minliang Lai and Letian Dou contributed equally to this work. *e-mail: p_yang@berkeley.edu

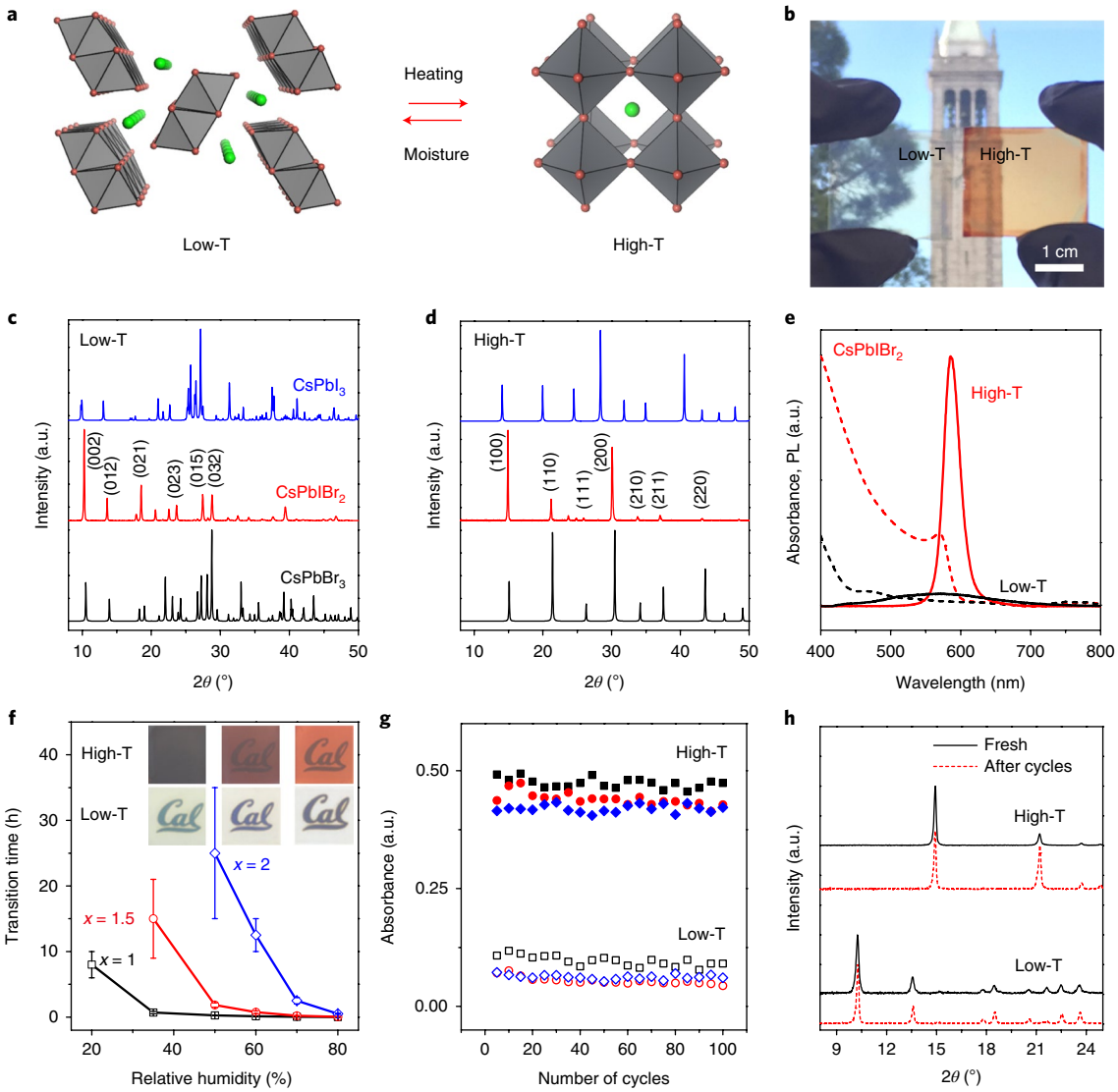

Fig. 1 | Phase transitions of inorganic halide perovskites. a, Schematics of the low-T to high-T phase transition by heating and the high-T to low-T transition by exposure to moisture. Caesium and halide atoms are shown in green and red, respectively. The low-T phase is represented by one-dimensional chains of edge-sharing lead-halide octahedra, whereas in the high-T phase the octahedra share corners. **b**, Photograph of the low-T phase (non-coloured) and high-T phase (orange-red-coloured) thin films. **c**,**d**, Powder X-ray diffraction (XRD) patterns of the $CsPbIBr_2$ (red) low-T (**c**) and high-T films (**d**) deposited on a glass substrate compared with the simulated $CsPbI_3$ (blue) and $CsPbBr_3$ (black) low-T orthorhombic and high-T cubic phases. **e**, Absorption (dashed lines) and PL (solid lines) spectra of the low-T (black) and high-T (red) $CsPbIBr_2$ films. **f**, Variation of the high-T to low-T phase transition time of $CsPbI_{3-x}Br_x$ films measured at different humidity conditions with RH = 20–80%. Error bars indicate the standard deviation. The inset shows the corresponding photographs of the high-T and low-T phase thin films (from left to right: $x = 1$, 1.5, and 2). The high-T phase films display different colours from dark brown to orange-red, while the low-T phase ones are fully transparent. **g**, The stable and reversible switching of the absorption (550 nm) of the three $CsPbIBr_2$ thin films over 100 phase transition cycles. **h**, XRD patterns of the low-T (black) and high-T (red) phase films before and after 100 cycles of phase transitions, showing full reversibility of the crystal structures.

achieving full phase reversibility is the back-conversion of the high-T to low-T phase. It is known that the metastable high-T phase of $CsPbI_3$ can be transitioned to the low-T phase by reheating to about 200 °C in an inert atmosphere[19]. When Br is added, the high-T phase is more stable, and difficult to revert to the low-T phase by mild heating. Instead, we find that, in general, moisture exposure effectively triggers this phase transition at room temperature. Methanol and ethanol vapours can also trigger the phase transition, but not as efficiently as moisture (Supplementary Fig. 1a). Fig. 1b shows the visually distinct images of the non-coloured low-T and orange-red-coloured high-T phase $CsPbIBr_2$ films, suitable for window applications. These transition processes could be potentially leveraged during normal device operation where sunlight is used to heat the film and drive off moisture (or assisted by extra heating), inducing a phase transition to the photovoltaically active high-T phase, while moisture ingress results in a subsequent phase transition back to the transparent low-T phase.

We use $CsPbIBr_2$ as a model system to characterize in detail the low-T and high-T phases. The powder X-ray diffraction (XRD) pattern of $CsPbIBr_2$ in the low-T phase matches well with the simulated pure iodide ($CsPbI_3$) and bromide ($CsPbBr_3$) low-T orthorhombic phases, with the corresponding peak positions sitting between them (Fig. 1c). The crystal structural details of $CsPbIBr_2$ are derived from rotation electron diffraction (RED) combined with fitting of the XRD pattern, identifying the low-T phase with space group *Pmnb* and $a = 4.797$ Å, $b = 9.982$ Å, $c = 17.184$ Å

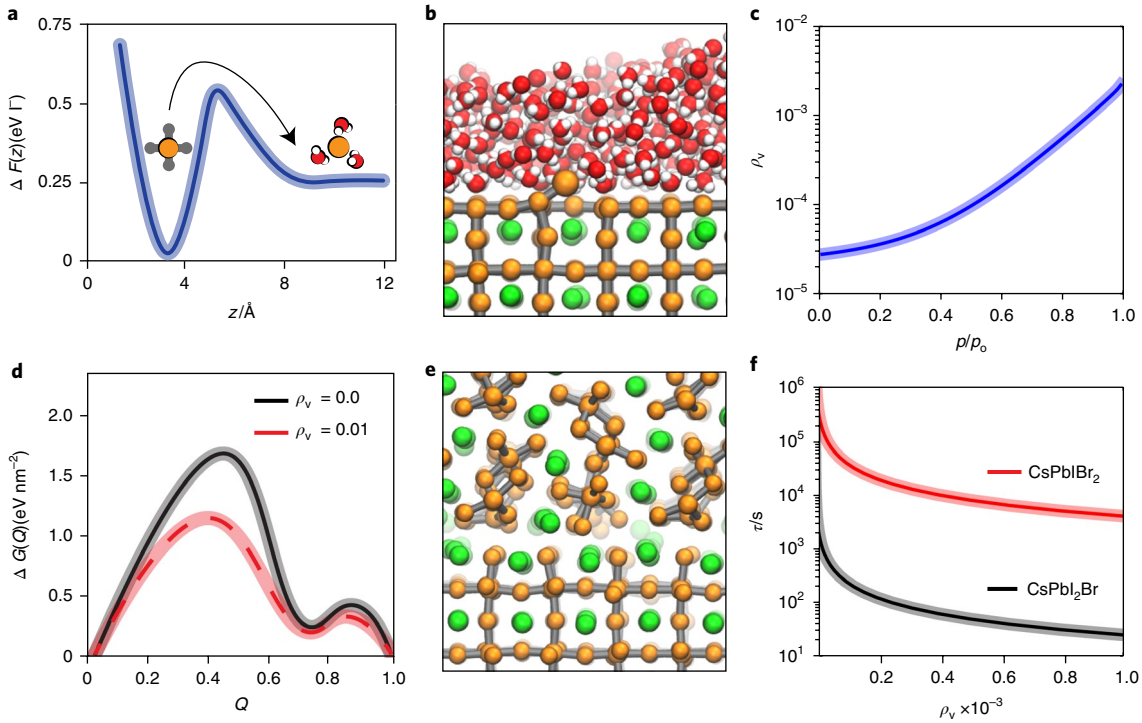

Fig. 2 | Mechanism of the moisture-triggered phase transition in inorganic perovskites. a, Reversible work, $\Delta F(z)$, to transfer an I^- atom from the solid perovskite to the thin adsorbed water layer, where z is the direction perpendicular to the interface. **b**, Snapshot from a molecular dynamics simulation near the top of the barrier in **a** showing the lead halide sub-lattice in grey and orange, the Cs^+ ions in green, the oxygens of the water in red and their hydrogens in white. **c**, Vacancy concentration, ρ_v, per unit cell as a function of relative humidity, p/p_o. **d**, Free energy to transform the high-T phase into the low-T phase, $\Delta G(Q)$, with or without an I^- vacancy, where Q is an order parameter that interpolates between the two crystal phases. **e**, Snapshot from a molecular dynamics simulation of the interface between the low-T and high-T phases with the same colouring as in **b**. **f**, Average nucleation time, τ, as a function of vacancy concentration for $CsPbIBr_2$ and $CsPbI_2Br$.

(Supplementary Fig. 2). A similar peak shift has been observed for the $CsPbIBr_2$ high-T phase as compared to the $CsPbI_3$ and $CsPbBr_3$ cubic phases (Fig. 1d). The unit cell of the high-T phase is determined to be $a = 5.926$ Å with the space group $Pm\text{-}3m$ (Supplementary Fig. 3 and Table 1). The large changes in the crystallographic structures indicate the first-order nature of the phase transition. The phenomenon of phase transition is different from the other observed transition behaviours between different colour states in halide perovskites accompanied by chemical reactions and new compound formation[20]. During the high-T to low-T transition process, the characteristic high-T XRD peak gradually diminishes while the low-T peak appears upon continuous exposure to moisture, and finally the high-T peak completely vanishes, indicating full conversion to the low-T phase (Supplementary Fig. 1b). Accordingly, the film shows a macroscopically homogeneous and gradual colour change across the entire region (Supplementary Fig. 1c and Supplementary Videos 1, 2) that tracks well with the XRD data. Fig. 1e quantitatively shows the optical absorption and PL spectra of the high-T and low-T phase thin films with light absorption above the band edge at about 2.1 and 2.9 eV, respectively. In the PL emission spectra, the high-T phase shows a narrow band edge emission, whereas the emission becomes much broader and weaker for the low-T phase.

The high-T to low-T phase transition rate is found to be strongly dependent on the composition ($x = 1$, 1.5 and 2) and relative humidity (RH = 20–80%, Fig. 1f). The inset in Fig. 1f shows the photographs of both the high-T and low-T phase films. The reversibility of the structural transitions between the low-T and high-T phases of the inorganic perovskite $CsPbIBr_2$ is monitored by the absorption spectra, which show no apparent changes after more than 100 repeated cycles (see Fig. 1g). Furthermore, no shift of the characteristic peaks or emergence of any impurity peaks (such as CsI, CsBr, PbI_2 or $PbBr_2$) is observed in the XRD patterns of either phase after repeated phase transition cycles (Fig. 1h). It is worth noting that, as compared to the freshly prepared high-T phase film, the (110)/(100) peak intensity ratio initially increases and subsequently remains stable during cycling, corresponding to a phase-transition-induced variation of the $CsPbIBr_2$ thin-film morphology, but without a significant change of the top surface roughness and grain dimensions (Supplementary Fig. 4). This observation can be explained by the rearrangement of crystal orientations in the thin film to reach the lowest surface energy.

The moisture adsorbed on the inorganic halide perovskite film surface can effectively catalyse the high-T to low-T phase transition at room temperature by introducing vacancies into the crystal lattice and lowering the free-energy barrier to nucleation[21]. Shown in Fig. 2a, free-energy calculations of a molecular model of $CsPbI_3$ show that there is a significant enhancement of halide vacancies when a thin water film is in contact with the perovskite interface[22], as pictured in Fig. 2b. This is a consequence of the large solvation enthalpy of halide ions and their accompanying low vacancy formation energy[23]. The characteristic time for a vacancy to be created at the interface is computed to be 1 ms, with an equilibrium concentration that depends on the relative humidity as in Fig. 2c and is up to five orders of magnitude larger than the expected defect concentration in the bulk of the material. Additional free-energy calculations shown in Fig. 2d report that there is a significant reduction of the surface tension between the low-T and high-T structures in the presence of halide vacancies. This reduction results from mitigating the ionic bonding constraints within the interfacial region of the lead-halide octahedra, which share corners in the high-T phase but share edges

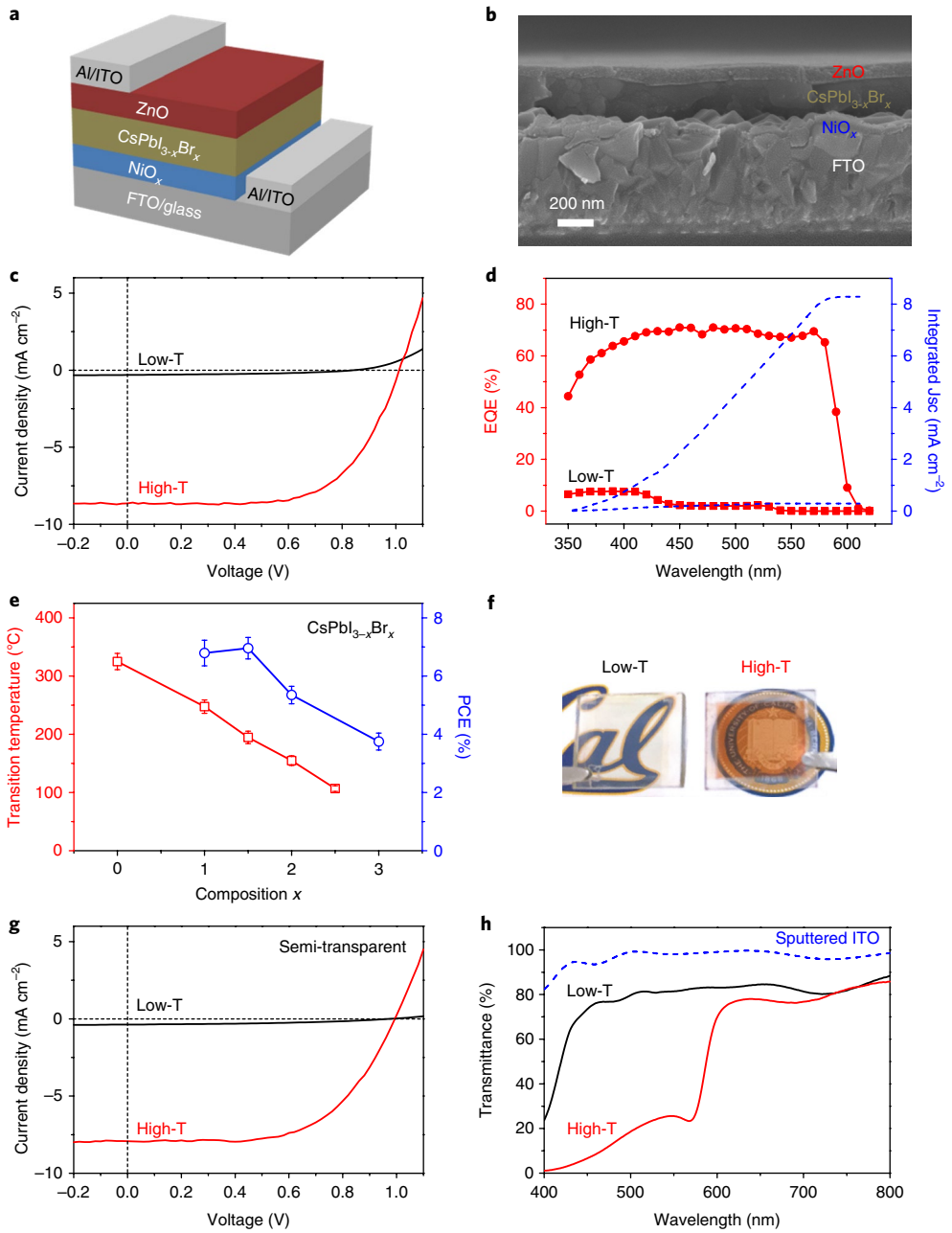

Fig. 3 | Characterization of phase transition solar cell devices. a, Schematic drawing of the solar cell architecture of glass/FTO/NiO_x/$CsPbI_{3-x}Br_x$/ZnO/Al or ITO. **b**, Cross-sectional scanning electron microscopy (SEM) image showing the homogenous and pinhole-free absorber active layer and the high-quality ZnO layer (without top electrode). **c**, Photocurrent density-voltage (*J*–*V*) characteristics of both the high-T and low-T phase solar cells (Al electrode) using $CsPbIBr_2$ as the active component (reverse scan at 20 mV s^{-1}), proving that the solar cell performance is greatly affected by the phase transition process. **d**, The external quantum efficiency (EQE) spectra and integrated J_{SC}. The integrated EQE matches the measured J_{SC} data to within 4%. **e**, The low-T to high-T phase transition temperature and solar cell performance (reverse scan at 20 mV s^{-1}) as a function of composition. Error bars indicate the standard deviation. A very high bromide concentration ($x > 2.5$) results in the stabilization of the high-T phase at room temperature, which can hardly be fully reverted back to the low-T phase. **f**, The image of the semi-transparent $CsPbIBr_2$ solar cell device in the (left) transparent mode and (right) orange-red-coloured photovoltaic mode with the sputtered ITO as the top transparent electrode. **g**, *J*–*V* curves of the semi-transparent device. **h**, The transmittance spectra of the semi-transparent device in the low-T (black curve) and high-T (red curve) phases. The transmittance of the sputtered ITO layer (thickness ~120 nm) is also given for reference.

in the low-T phase (see Fig. 2e). This reduction of the free-energy barrier to nucleation at the sites of halide vacancies results in a transition rate that changes exponentially in the presence of a vacancy, as quantified in Fig. 2f for $CsPbIBr_2$ and $CsPbI_2Br$. The moisture triggered phase transition was further characterized by ambient pressure X-ray photoemission spectroscopy (AP-XPS). When exposing to water vapour, the adsorbed oxygen amount on surface increases but does not change with the probing depth (Supplementary Fig. 5), indicating that water is adsorbed only on the surface without penetrating interior of the lattice. The results reveal that the phase transition is fundamentally different from the hydration/dehydration process observed in hybrid perovskite $MAPbI_3$ [24–26], which suffers from decomposition after water molecule intercalation.

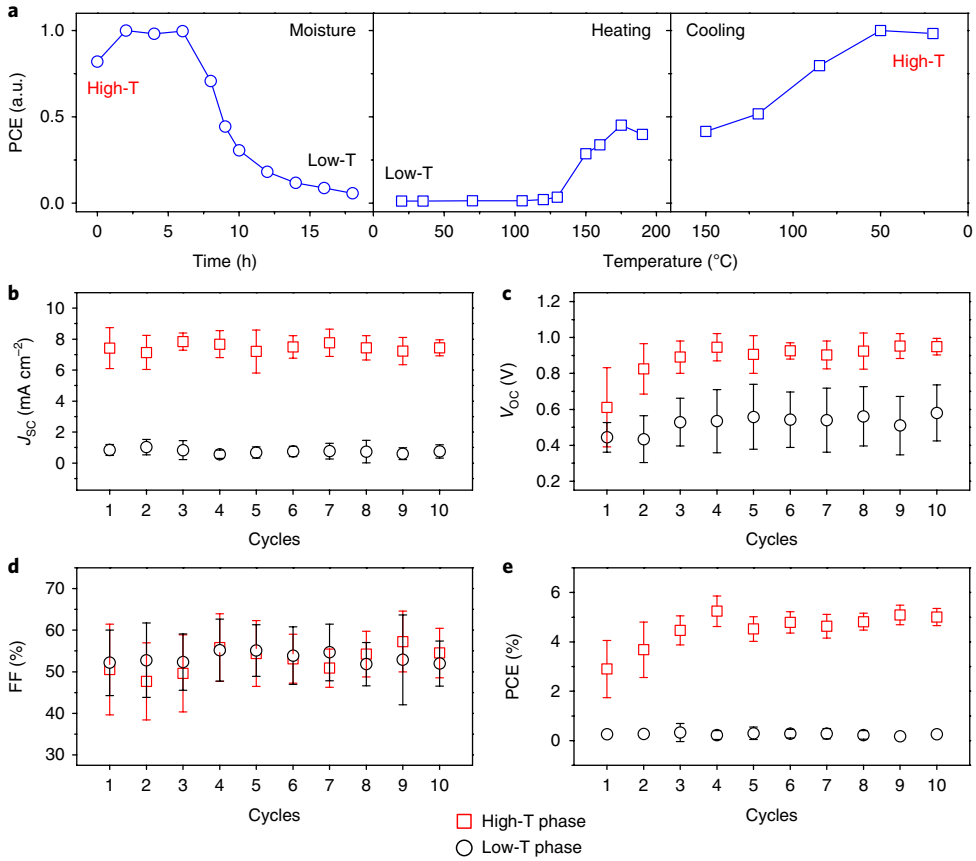

Fig. 4 | The evolution and reversibility of photovoltaic properties during phase transition cycles. a, In situ observation of the time-dependent performance of a $CsPbIBr_2$ solar cell from high-T to low-T phase at RH = 60%, and temperature-dependent device performance from low-T to high-T phase by heating. **b–e**, Short-circuit current density (J_{SC}) (**b**), open-circuit voltage (V_{OC}) (**c**), fill factor (FF) (**d**), power conversion efficiency (PCE) (**e**) of devices over 10 transition cycles between the high-T (red squares) and low-T (black circles) phases. Error bars indicate the standard deviation; 10 separate $CsPbIBr_2$ cells were used. The slight fluctuation is associated with different perovskite film crystallinity during each heating cycle.

To achieve solar cell devices with switchable power output utilizing the phase transitions, a sufficiently robust architecture that can withstand the moisture or heating treatment needs to be designed. Initially, we have explored the use of typical organic interlayer materials in devices (see Methods), but they undergo a severe irreversible thermal degradation upon heating above 150 °C. By applying solution-processed high-quality metal oxide-based hole and electron extraction layers[27–29], an all-inorganic solar cell using an inverted planar p-i-n heterojunction geometry consisting of glass/fluorine-doped tin oxide (FTO)/NiO_x (~80 nm)/$CsPbI_{3-x}Br_x$ (~200 nm)/ZnO (~70 nm)/Al (Fig. 3a,b) is realized that maximizes the thermal and environmental stability. The overall surface roughness after coating with dense ZnO nanoparticles is as low as ~7 nm. Fig. 3c shows the J–V curves, with the solar cell based on $CsPbIBr_2$ in the high-T phase showing an open-circuit voltage (V_{OC}) of 1.01 V, a short-circuit current density (J_{SC}) of 8.65 mA cm^{-2}, and a fill factor (FF) of 63.6%, corresponding to a power conversion efficiency (PCE) of 5.57%. The same cell after switching to the low-T phase exhibits a V_{OC} of 0.84 V, a J_{SC} of 0.31 mA cm^{-2}, an FF of 43.9%, and a PCE of 0.11%. A ~50-fold difference in PCE between the two phases is observed. The device in the high-T phase shows a low J–V hysteresis with respect to the scan direction and gives a stabilized power output of 5.10% under continuous one-sun illumination (Supplementary Fig. 6 and Table 2). According to the external quantum efficiency (EQE) measurements shown in Fig. 3d, the photocurrent onsets are at approximately 590 and 430 nm for the high-T and low-T phases, respectively.

For mixed halide perovskite $CsPbI_{3-x}Br_x$ ($0 \leq x \leq 3$), the bandgap of the high-T phase can be tuned continuously in the range 1.7–2.3 eV by controlling the bromide to iodide ratio in the alloy (Supplementary Fig. 7a). The corresponding solar cell devices show the peak PCEs above 7% (for $x = 1$, 1.5, Fig. 3e, Supplementary Fig. 7b and Table 3). Although $CsPbI_3$ has a more desirable bandgap for photovoltaics, the device shows a low PCE, probably due to the high phase instability at room temperature. As x increases ($0 \leq x \leq 2.5$), the phase transition temperature decreases nearly linearly from 320 to 105 °C (Fig. 3e). The structural phase transition was further confirmed by variable-temperature grazing-incidence wide-angle X-ray (GIWAX) diffraction (see Supplementary Fig. 8). On the other hand, the high-T phase becomes more stable against moisture with increasing x (Fig. 1f). For $CsPbBr_3$, moisture treatment at room temperature does not result in the low-T phase, probably because the high-T phase is thermodynamically more stable at ambient conditions[30].

Approaches towards semi-transparent devices were further explored with the replacement of Al with transparent top electrodes to study the compatibility with the transparent conductive layers[31–33]. A 50 nm layer of solution-processed Al-doped ZnO was applied as the buffer layer on top of the ZnO, followed by sputtering a 120-nm-thick indium tin oxide (ITO) to form the top transparent electrode (see Methods). After post annealing of the complete device at approximately 200 °C, the ITO layer shows a high transparency. Fig. 3f shows the images of the devices based on a transparent ITO top layer at the low-T and high-T phases, respectively. The high-T phase device yields a V_{OC} of 1.00 V, a J_{SC} of 7.92 mA cm^{-2}, an

FF of 59.2%, a PCE of 4.69%, and a stabilized power output of 4.29%, while the low-T phase shows a V_{OC} of 0.97 V, a J_{SC} of 0.37 mA cm^{-2}, an FF of 41.6%, and a PCE of 0.15% (Fig. 3g and Supplementary Fig. 9a, b). Unlike the 'yellow phase' $CsPbI_3$, the low-T phase of $CsPbIBr_2$ is fully transparent (Supplementary Fig. 7c). The device at these two phases shows distinct average degrees of visible transparency of 81.7% and 35.4%, respectively (Fig. 3h). The successful deposition of ITO also indicates that the thermal stability of the inorganic perovskite-based devices is an intriguing feature for potential applications as high-temperature stable solar cells that can withstand harsh device-processing conditions[34].

For cycling tests, the composition $CsPbIBr_2$ was used due to its relatively low phase transition temperature (150 °C), high device stability, and good visual characteristics for window applications. The photovoltaic parameters in one phase transition cycle were monitored in situ (Fig. 4a and Supplementary Fig. 10). In the initial stage of the high-T to low-T phase transition by moisture treatment, the device PCE was stable and even slightly enhanced, possibly due to the vacancy accumulation process. Afterwards, the PCE gradually decreased, corresponding to the phase-transition nucleation and propagation, before reaching a stabilized low value indicating full conversion to the low-T phase. For the low-T to high-T transition, the device was gradually heated up to 190 °C and then cooled to room temperature in the ambient atmosphere. The PCE increases sharply (more than 8-fold) when approaching 150 °C, which suggests the beginning of the phase transition. A further increase in the temperature results in the improved PCE, likely as a result of the slow phase transition propagation within the film, before the PCE starts to decay at above 175 °C. Upon cooling, the PCE actually gradually increases back to the original value. For a complete cycle, according to our estimation by considering the heating, enthalpy change, and heat loss for the phase transition process, the smart photovoltaic window could achieve a positive net energy balance, provided lower transition temperatures (around 100 °C) and faster cycling times (<10 min) are achieved.

Fig. 4b–e shows the statistical analysis of the change in solar cell performance parameters over repeated phase transition cycles. Performance variations of individual solar cells are shown in Supplementary Fig. 11. The characteristic parameters J_{SC}, V_{OC}, FF, and PCE all show a reversible behaviour. In each cycle, the J_{SC} and PCE drop sharply when the device turns to the low-T phase by moisture treatment before full recovery by heating. The J_{SC} of the high-T phase (solar cell operating phase) keeps relatively stable over 10 cycles, which is attributed to the reversible optoelectronic properties of the absorber layer. The initial PCE in the high-T phase is relatively low, and increases gradually in the first two or three cycles. This is directly related to an increase in the V_{OC} at the initial stage, and likely due to the preferred crystal orientation and passivation of the grain boundaries[35,36]. After reaching steady state, the device performance of the high-T phase shows no obvious degradation during cycling. The evolution of the solar cell parameters between the low-T and high-T phases is in good agreement with the above in situ results. Finally, as an example, we find that, for the semi-transparent device (Supplementary Fig. 9c), more than 85% of the peak PCE is retained after up to 40 repeated cycles of transitions, with no clear downward trend, indicating the high thermal and environmental stability of the all-inorganic solar cells.

We have demonstrated the thermochromic solar cell as a smart photovoltaic window that is realized by controlled transitions between the inorganic perovskite low-T and high-T phases. The solar cell features high thermal stability and fully reversible colour and performance, which are key requirements for successful integration into diverse applications. This phase transition photovoltaic technique has the potential to be extended to other types of halide perovskite composites and nanometre-sized structures featuring more ideal bandgaps for higher power output, lower phase transition temperatures for self-adaptive transparency, and more robust device architectures for long-term stability. Our results indicate that halide perovskites are not only ideal for low-cost and high-efficiency solar cells, but also possess rich phase change behaviours for switchable optoelectronics.

Methods

Methods, including statements of data availability and any associated accession codes and references, are available at https://doi.org/10.1038/s41563-017-0006-0.

Received: 15 June 2017; Accepted: 29 November 2017;
Published online: 22 January 2018

References

1. Baetens, R., Jelle, B. P. & Gustavsen, A. Properties, requirements and possibilities of smart windows for dynamic daylight and solar energy control in buildings: A state-of-the-art review. *Sol. Energy Mater. Sol. Cells* **94**, 87–105 (2010).
2. Niklasson, G. A. & Granqvist, C. G. Electrochromics for smart windows: thin films of tungsten oxide and nickel oxide, and devices based on these. *J. Mater. Chem.* **17**, 127–156 (2007).
3. Lampert, C. M. Chromogenic smart materials. *Mater. Today* **7**, 28–35 (March, 2004).
4. Chen, C.-C. et al. Visibly transparent polymer solar cells produced by solution processing. *ACS Nano* **6**, 7185–7190 (2012).
5. Eperon, G. E., Burlakov, V. M., Goriely, A. & Snaith, H. J. Neutral color semitransparent microstructured perovskite solar cells. *ACS Nano* **8**, 591–598 (2014).
6. Bechinger, C., Ferrer, S., Zaban, A., Sprague, J. & Gregg, B. A. Photoelectrochromic windows and displays. *Nature* **383**, 608–610 (1996).
7. Lampert, C. Large-area smart glass and integrated photovoltaics. *Sol. Energy Mater. Sol. Cells* **76**, 489–499 (2003).
8. Cannavale, A. et al. Perovskite photovoltachromic cells for building integration. *Energy Environ. Sci.* **8**, 1578–1584 (2015).
9. Morin, F. Oxides which show a metal-to-insulator transition at the Neel temperature. *Phys. Rev. Lett.* **3**, 34–36 (1959).
10. Hosseini, P., Wright, C. D. & Bhaskaran, H. An optoelectronic framework enabled by low-dimensional phase-change films. *Nature* **511**, 206–211 (2014).
11. Grätzel, M. The light and shade of perovskite solar cells. *Nat. Mater* **13**, 838–842 (2014).
12. Li, X. et al. A vacuum flash–assisted solution process for high-efficiency large-area perovskite solar cells. *Science* **353**, 58–62 (2016).
13. Quarti, C. et al. Structural and optical properties of methylammonium lead iodide across the tetragonal to cubic phase transition: implications for perovskite solar cells. *Energy Environ. Sci.* **9**, 155–163 (2016).
14. Stoumpos, C. C., Malliakas, C. D. & Kanatzidis, M. G. Semiconducting tin and lead iodide perovskites with organic cations: phase transitions, high mobilities, and near-infrared photoluminescent properties. *Inorg. Chem.* **52**, 9019–9038 (2013).
15. Eperon, G. E. et al. Inorganic caesium lead iodide perovskite solar cells. *J. Mater. Chem. A* **3**, 19688–19695 (2015).
16. Swarnkar, A. et al. Quantum dot–induced phase stabilization of α-$CsPbI_3$ perovskite for high-efficiency photovoltaics. *Science* **354**, 92–95 (2016).
17. Sharma, S., Weiden, N. & Weiss, A. Phase diagrams of quasibinary systems of the type: ABX_3—$A'BX_3$; ABX_3—$AB'X_3$, and ABX_3—ABX'_3; X=Halogen. *Phys. Chem.* **175**, 63–80 (1992).
18. Møller, C. K. Crystal structure and photoconductivity of caesium plumbohalides. *Nature* **182**, 1436 (1958).
19. Lai, M. et al. Structural, optical, and electrical properties of phase-controlled cesium lead iodide nanowires. *Nano Res.* **10**, 1107–1114 (2017).
20. De Bastiani, M. et al. Thermochromic perovskite inks for reversible smart window applications. *Chem. Mater.* **29**, 3367–3370 (2017).
21. Dastidar, S. et al. High chloride doping levels stabilize the perovskite phase of cesium lead iodide. *Nano Lett.* **16**, 3563–3570 (2016).
22. Mattoni, A., Filippetti, A. & Caddeo, C. Modeling hybrid perovskites by molecular dynamics. *J. Phys. Condens. Mat.* **29**, 043001 (2016).
23. Kang, J. & Wang, L.-W. High defect tolerance in lead halide perovskite $CsPbBr_3$. *J. Phys. Chem. Lett.* **8**, 489–493 (2017).
24. Christians, J. A., Miranda Herrera, P. A. & Kamat, P. V. Transformation of the excited state and photovoltaic efficiency of $CH_3NH_3PbI_3$ perovskite upon controlled exposure to humidified air. *J. Am. Chem. Soc.* **137**, 1530–1538 (2015).
25. Leguy, A. M. et al. Reversible hydration of $CH_3NH_3PbI_3$ in films, single crystals, and solar cells. *Chem. Mater.* **27**, 3397–3407 (2015).

26. Halder, A., Choudhury, D., Ghosh, S., Subbiah, A. S. & Sarkar, S. K. Exploring thermochromic behavior of hydrated hybrid perovskites in solar cells. *J. Phys. Chem. Lett.* **6**, 3180–3184 (2015).
27. You, J. et al. Improved air stability of perovskite solar cells via solution-processed metal oxide transport layers. *Nat. Nanotechnol.* **11**, 75–81 (2016).
28. Kim, J. H. et al. High-performance and environmentally stable planar heterojunction perovskite solar cells based on a solution-processed copper-doped nickel oxide hole-transporting layer. *Adv. Mater.* **27**, 695–701 (2015).
29. Song, J. et al. Efficient and environmentally stable perovskite solar cells based on ZnO electron collection layer. *Chem. Lett.* **44**, 610–612 (2015).
30. Marstrander, A. & Møller, C. K. The structure of white cesium lead (II) bromide, $CsPbBr_3$. *Mat. Fys. Medd. Dan. Vid. Selsk* **35**, 1–12 (1966).
31. Dou, L. et al. Solution-processed copper/reduced-graphene-oxide core/shell nanowire transparent conductors. *ACS Nano* **10**, 2600–2606 (2016).
32. Bush, K. A. et al. Thermal and environmental stability of semi-transparent perovskite solar cells for tandems enabled by a solution-processed nanoparticle buffer layer and sputtered ITO electrode. *Adv. Mater.* **28**, 3937–3943 (2016).
33. Lang, F. et al. Perovskite solar cells with large-area CVD-graphene for tandem solar cells. *J. Phys. Chem. Lett.* **6**, 2745–2750 (2015).
34. Divitini, G. et al. In situ observation of heat-induced degradation of perovskite solar cells. *Nat. Energy* **1**, 15012 (2016).
35. Eperon, G. E. & Ginger, D. S. Perovskite solar cells: Different facets of performance. *Nat. Energy* **1**, 16109 (2016).
36. Chen, Q. et al. Controllable self-induced passivation of hybrid lead iodide perovskites toward high performance solar cells. *Nano Lett.* **14**, 4158–4163 (2014).

Acknowledgements

This work is primarily supported by the U.S. Department of Energy, Office of Science, Basic Energy Sciences, Materials Sciences and Engineering Division under contract no. DE-AC02-05CH11231 (PChem KC3103). The GIWAX data were collected at the Stanford Synchrotron Radiation Light Source at SLAC National Accelerator Laboratory supported by the U.S. Department of Energy, Office of Science, Basic Energy Sciences under contract no. DE-AC02-76SF00515. The XPS data was collected at the Advanced Light Source, with help from E.J. Crumlin, Q.Kong and H.Zhang, which is a DOE Office of Science User Facility under contract no. DE-AC02-05CH11231. The RED data was collected at the Berzelii Center EXSELENT on Porous Materials, the Swedish Research Council (Grant no. 2012-4681). J.L. acknowledges the fellowship support from Shanghai University of Electric Power. M.L. and C.X. acknowledges the fellowship support from Suzhou Industrial Park. C.S.K. acknowledges support by the Alexander von Humboldt Foundation. H.C. acknowledges the postdoctoral scholarship support from the Wallenberg Foundation through the MAX IV synchrotron radiation facility program. D.L. thanks the Camille and Henry Dreyfus Foundation for funding, Award EP-14-151. S.A.H. acknowledges the support from the DOE Office of Energy Efficiency and Renewable Energy (EERE) Postdoctoral Research Award under the EERE Solar Energy Technologies Office administered by the Oak Ridge Institute for Science and Education (DE-AC05-06OR23100). We thank M.F. Toney for discussions on the GIWAX data, Y. Wang for the work on the supplementary videos, and J. Kanady for proofreading the manuscript.

Author contributions

J.L., M.L., L.D. and P.Y. conceived the idea and designed the study. J.L., M.L. and L.D. contributed to all the experimental work. C.S.K. performed the AFM measurements. H.C., F.P. and J.S. carried out the RED experiments and data analysis. D.L., S.A.H., C.X. and F.C. helped with the device characterizations. D.T.L. performed the molecular modeling. J.L. and P.Y. wrote the manuscript. All authors discussed the results and revised the manuscript.

Competing interests

The authors declare no competing financial interests.

Additional information

Supplementary information is available for this paper at https://doi.org/10.1038/s41563-017-0006-0.

Reprints and permissions information is available at www.nature.com/reprints.

Correspondence and requests for materials should be addressed to P.Y.

Publisher's note: Springer Nature remains neutral with regard to jurisdictional claims in published maps and institutional affiliations.

Methods

Oxide and perovskite film deposition. Unless otherwise stated, all chemicals were purchased from Sigma-Aldrich Chemical and used as received. Nickel oxide (NiO_x) film was prepared as follows. 0.1 M nickel (II) acetate tetrahydrate with 0.1 M ethanolamine was mixed in ethanol, and stirred at 70 °C for 3 h. The precursor solution was spin-coated on pre-patterned FTO glass at 2,000 r.p.m. for 60 s. Then the substrate was annealed at 270 °C for 30 min. Afterwards, the substrate was transferred to a N_2-filled glovebox for further processing. Mixed halide $CsPbI_{3-x}Br_x$ thin film ($0 \leq x \leq 2$) was prepared by a single-step method, in which 0.5 M caesium lead halide precursor solution was prepared by mixing appropriate amounts of CsI, CsBr, PbI_2 and $PbBr_2$ powders (99.999%) into *N*,*N*-dimethylformamide (DMF) or dimethylsulfoxide (DMSO). The solution was stirred for 2 h and filtrated by 0.2 μm polytetrafluoroethylene (PTFE) filter syringes before use. Then the solution was spin-coated onto a NiO_x layer at 1,500 r.p.m. for 90 s. The thin film was annealed at different temperatures for 10 min. For a more bromide-rich $CsPbI_{3-x}Br_x$ thin film ($x > 2$), a two-step method was adopted, in which 1 M $PbBr_2$ in DMF was spin-coated at 4,000 r.p.m. onto the NiO_x layer, and then heated at 75 °C for 30 min. The perovskite film was grown by dipping the $PbBr_2$ film in 8–16 mg ml^{-1} methanol solution with different CsBr:CsI mole ratios at a solution temperature of 75 °C for 10 min, and then washing immediately with 2-propanol (IPA) for 30 s. The substrate was then dried by heating to 135 °C for 10 min. The two-step method generated a nanocuboid film morphology. Zinc oxide (ZnO) nanoparticles were prepared in methanol via hydroxylation of zinc acetate by potassium hydroxide[37]. The as-prepared ZnO nanoparticles (~4 nm size) were redispersed in chloroform with a 2 wt.% concentration, spin-coated on the perovskite surface at 4,000 r.p.m. for 10 s, and then annealed at 75 °C for 10 min.

Devices. The inverted p-i-n (deposition order) device with the glass/FTO/NiO_x/$CsPbI_{3-x}Br_x$/ZnO/Al structure was fabricated. A 100-nm-thick Al electrode was thermally evaporated through a shadow mask under a high vacuum of ~5×10^{-7} torr at a rate of 0.1 nm s^{-1}. The semi-transparent device was fabricated by replacing the Al electrode with a sputtered indium tin oxide (ITO) layer. First, 2.5 wt.% Al-doped ZnO with an average particle size of 15 nm in IPA was spin coated on the ZnO surface at 4,000 r.p.m. for 10 s, followed by annealing at 75 °C for 10 min as a buffer layer. Afterwards, a 120 nm ITO layer was prepared by radiofrequency sputtering, with a sputtering rate of 9.6 nm s^{-1} and a power of 120 W as determined by thickness calibration of sample films. The base pressure of the chamber was 2×10^{-5} torr and the Ar pressure was fixed at 18 mtorr. The ITO layer was post annealed in air at 200 °C for 30 min. For the glass/FTO/NiO_x/$CsPbI_{3-x}Br_x$/PCBM/Al device architecture, [6,6]-phenyl-C_{61}-butyric acid methyl ester (PCBM, 20 mg ml^{-1} in chlorobenzene) was used as the electron transport material by spin-coating at 1,200 r.p.m. for 60 s. For n-i-p devices, the glass/FTO/TiO_2/$CsPbI_{3-x}Br_x$/spiro-OMeTAD/Au structure was used. First, 0.15 M titanium diisopropoxide bis(acetylacetonate) in 1-butanol was spin-coated on FTO glass at 2,000 r.p.m. for 60 s, followed by annealing at 500 °C for 20 min to form a compact TiO_2 layer. A 200 nm mesoporous TiO_2 layer was cast by spin-coating a 1:7 diluted TiO_2 paste (Dyesol) at 1,500 r.p.m. for 60 s, and then annealed at 500 °C for 20 min. 2,2′,7,7′-tetrakis-(*N*,*N*-di-4-methoxyphenylamino)-9,9′-spirobifluorene (Spiro-OMeTAD, 75 mg in 1 ml chlorobenzene) was doped with 17 μl 4-tert-butylpyridine (TBP) and 30 μl Li-TFSI stock solution (170 mg ml^{-1} in acetonitrile), and then spin-coated on the perovskite layer at 4,000 r.p.m. for 60 s. A 100-nm-thick Au was evaporated at a rate of 0.02 nm s^{-1}.

Heating/moisture treatment. The perovskite film and device were treated by heating or moisture exposure without encapsulation. The heating process was conducted in the glovebox, on a hotplate with ramping rate of 20 °C min^{-1}, and then held at the corresponding temperatures for 10 min to allow equilibrium or complete transition. The temperature was calibrated by a digital thermometer. The moisture treatment was conducted in a humidity control box with flowing N_2 gas containing moisture at room temperature ($N_2 + H_2O$, 20 ± 1 °C). The relative humidity (RH) was controlled in the range 20–80% (± 5%).

Phase transition temperature/rate. The low-T to high-T phase transition temperature and high-T to low-T transition rate were determined by the colour change of the thin films, which is indicative of phase transition, and the crystal phase was confirmed by powder X-ray diffraction (XRD, Bruker D8, Cu K_α radiation, 1.54056 Å) analysis. XRD spectra were also taken at intervals in the high-T to low-T phase transition process to monitor the changes in the crystal phase. GIWAX data of the low-T to high-T transition were collected at SSRL beamline I11-3. The sample was heated in situ on a hot plate in a helium chamber.

Crystal structures. Three-dimensional electron diffraction data were collected by using a rotation electron diffraction (RED) data collection program on a JEOL JEM-2100 transmission electron microscope[38]. Transmission electron microscopy (TEM) bright-field images and energy dispersive spectra were also collected on the same TEM. The dried film was scratched from the glass substrate and then coated on a copper grid with the carbon film (STEM150 Cu grids, Okenshoji) directly. The collection angle ranges from −35° up to +35°. The goniometer tilt step is 2°, and the beam tilt step is 0.2°, with a beam tilt range of ± 1.0°. The data collection was performed at room temperature. The three-dimensional reciprocal lattice was reconstructed from the RED data for the low-T and high-T phases. On the basis of the three-dimensional data, combined with Le Bail fitting of XRD, the unit cell information was derived directly[39].

AP-XPS studies. Ambient pressure X-ray photoelectron spectroscopy (AP-XPS) was performed at the Lawrence Berkeley National Laboratory Advanced Light Source (ALS) Beamline 9.3.2. A VG-Scienta R4000 HiPP analyzer was used. Samples were prepared on silicon substrates, and XPS spectra were collected using incident X-ray energies of 630, 730, or 800 eV. The high-T phase sample was measured in ultrahigh vacuum and then in an atmosphere of H_2O (200 mtorr)/Ar (50 mtorr) to study the in situ high-T to low-T phase transition. The binding energy for XPS spectra was calibrated with reference to the adventitious C 1 s at 284.6 eV. The XPS spectra were analyzed by subtracting a Shirley background. After exposure to H_2O/Ar, the surface adsorbed O amount with different probing depths was indicated by the ratio of surface-adsorbed O to gaseous H_2O. The latter does not change with time due to the consistent H_2O partial pressure in the chamber.

Film characterization. The morphologies of films and devices were analyzed by a field-emission scanning electron microscope (FE-SEM, JEOL JSM-6340F). The size of nanoparticles was analysed by transmission electron microscopy (TEM, Hitachi H-7650). The transmittance and absorption spectra were obtained by means of an ultraviolet-visible spectrophotometer (UV-3101, Shimadzu). The luminous transparency of the film is characterized by the visible luminous transmittance (CIE 1931 human perception of transmittance) averaged over the spectral range 400–780 nm (ref. [40]):

$$T = \int_{400}^{780} I(\lambda)\varphi(\lambda)T(\lambda)\mathrm{d}\lambda \Big/ \int_{400}^{780} I(\lambda)\varphi(\lambda)\mathrm{d}\lambda \quad (1)$$

where $I(\lambda)$is the standard AM 1.5 power density distribution, $\varphi(\lambda)$is the spectral response of the human eye, and $T(\lambda)$ is the measured transmittance. Atomic force microscopy (AFM) measurements were performed on an AFM system (MFP-3D Asylum Research, Oxford Instruments) equipped with an acoustic isolation chamber (AEK 2002) in non-contact mode at room temperature in an inert atmosphere. Photoluminescence spectra were measured by using a 375 nm solid state laser (Coherent) as the excitation with its power adjustable by neutral density filters (normally 1–100 μW). The emitted light was collected by an optical objective (50×, NA = 0.55) and sent to the grating-based spectrograph (Princeton Instruments, SP-2300i) through an optical fibre for spectral analysis.

Device testing. The performance parameters of the devices were measured under full sunlight (AM 1.5 G, 100 mW cm^{-2}). A class A solar simulator (300 W, Oriel) was used for irradiation and the light intensity was calibrated with a Si reference cell (Mono-Si with KG5 filter, NIST). Photocurrent–voltage (*J*–*V*) curves were obtained by applying forward and reverse voltage scans using a source meter (Keithley 4200) without any device preconditioning. The scan rate was set at 20, 100 or 400 mV s^{-1}. The device active area was restricted to be 4 mm^2 by means of a metal mask. The stabilized power output was measured under continuous illumination over 400 s at the maximum power point. The temperature-dependent *J*–*V* curves were measured by placing the device on a hotplate and the temperature was allowed to equilibrate for 5 min. The external quantum efficiency (EQE) was measured by standard lock-in techniques. In brief, the device was excited by chopped (77 Hz) long-pass-filtered monochromatic light (Acton monochromator, Oriel 300 W Xenon lamp) while connected to a 50 Ω resistor in parallel with an SR830 lock-in amplifier. The resulting signal was converted into a quantum efficiency by comparison with a calibrated silicon photodiode (Newport 818) measured under identical conditions.

Molecular dynamics models. The molecular dynamics simulations were accomplished with force fields of the form of a Buckingham potential, as parameterized for $MgSiO_3$[41] and rescaled for $CsPbI_3$. Such models of $CsPbI_3$ are able to reproduce the experimental lattice constants and relative stabilities of different crystal structures. Interactions between water molecules were modelled with the SPC/E water[42] and ion water interactions were modelled with Lennard Jones potentials[43]. These parameters were chosen to recover known hydration energies for the ions, and provide an interfacial structure of water on $CsPbI_3$ that is consistent with ab initio studies[44]. Molecular simulations were run in LAMMPS[45] with initial conditions taken from known crystal structures. Integration of the equations of motion were done first in an NPT ensemble using a Parinello–Rahman barostat, for 100 ps, followed by 10 ns runs with NVT dynamics using a Langevin thermostat. Periodic boundary conditions were used in all cases. Calculations employing free interfaces accounted for the altered electrostatic environment using a slab-corrected Ewald summation. Unless otherwise noted, the calculations used a supercell of 10 × 10 × 10 perovskite $CsPbI_3$ unit cells. For the hydrated interfaces, we begin by simulating a bare surface with semi-Grand Canonical hybrid Monte Carlo, where the chemical potential is set by differing values of the relative humidity based on equilibrium vapour pressure calculations

from REF-DL[46]. We find that complete monolayer formation occurs only at 40% relative humidity. After 40% p/p_o, layering increases exponentially fast with increasing relative humidity, allowing us to assume that the ion concentration increases with the increasing volume of liquid.

Umbrella sampling calculations. Calculations to determine the free energy for transferring an I^- from a pristine PbI_2-terminated interface of the high-T phase of $CsPbI_3$ to an adsorbed thin water film were accomplished using umbrella sampling. These free-energy calculations were computed with 1,000 waters, in a region $5\times5\times12$ nm^3. This particular interface was studied, as it is known been shown the most stable to water[44], and as such is expected to set an upper bound for the transfer free energy relative to higher index interfaces, Cs^+-terminated surfaces, or defective surfaces. Similarly, I^- is more weakly hydrated than Br^-, so we would expect a large driving force for dissolution for Br^- over I^-. The umbrella sampling calculations were accomplished with harmonic biasing potentials, 15 simulations, spaced 0.5 Å apart and with a 10 kcal Å^{-2} spring constant and 5 additional windows with 0.2 spring constant near the top of the barrier, with a spring constant of 20 kcal Å^{-2}. The weighted histogram analysis method (WHAM) was used to unbias these simulations[47] and produce Fig. 2b. The Bennet-Chandler method[48] was used to compute the associated rate for dissolution, with transition state associated with the peak free energy along the direction perpendicular to the interfaces and a recrossing coefficient computed to be 0.1.

Finite temperature string calculations. In order to study the free energy required to transition between the low-T and high-T phases, shown in Fig. 2d, we used the finite-temperature string method. A much smaller system size of 24 $CsPbI_3$ unit cells was used to compute the free-energy profiles between the two phases. An initial interpolation between the two phases was produced using Wang–Landau sampling[49] with an order parameter, Q, defined as an interpolation between two overlap functions

$$Q[\mathbf{r}] = \theta(\mathbf{r}|\mathbf{r}_\alpha,\sigma)/(\theta[\mathbf{r}|\mathbf{r}_\alpha,\sigma]+\theta[\mathbf{r}|\mathbf{r}_\beta,\sigma]) \quad (2)$$

where $\mathbf{r}$ are the instantaneous coordinates of the system, $\mathbf{r}_\alpha$ are the equilibrium lattice coordinates for phase α and the overlap function is defined as

$$\theta[\mathbf{r}|\mathbf{r}_\alpha,\sigma] = \frac{1}{N}\sum_{i,j=1}^{N} e^{-\left(\mathbf{r}_i-\mathbf{r}_j^{(\alpha)}\right)^2/2\sigma^2} \quad (3)$$

where $\sigma = 1.5$ Å is small enough to ensure θ is bounded by 1. Initial simulations included only hard-core interactions between the molecules. Initial pathways produced in this way were used as initial conditions for the free-energy calculations that were evaluated by the finite-temperature string method[50] using 20 windows. Calculations required 1 ns for each window to converge. Calculations were done with initial strings parameterized with or without various defects and from both directions (low-T phase to high-T phase and vice versa) to ensure sampling hysteresis was mitigated. Only I^- defects were found to decrease the free energy. Pb^{2+} and Cs^+ defects increase the barrier heights to transformation. For these charged defects, electroneutrality was accomplished using a uniform neutralizing background charge. These calculations were compared with direct simulations to compute the excess interface energy of a variety of pristine solid–solid boundaries, which clarifies that the free-energy change has significant entropic character.

Given the large difference in the barrier to nucleation with and without a vacancy, we assume the characteristic transition time follows a simple model of heterogeneous nucleation. Specifically, we assume that the observed rate of interconversion is equal to the sum of the rate in the presence of the vacancy, times the vacancy concentration, plus the rate away from a vacancy, times one minus the vacancy concentration. We fit the data at different relative humidities for each composition, and use the free-energy calculations to predict the timescale for interconversion as a function of vacancy concentration, shown in Fig. 2f.

Data availability. The experimental and simulation data that support the findings of this study are available from the corresponding author upon request.

References

37. Sun, B. & Sirringhaus, H. Solution-processed zinc oxide field-effect transistors based on self-assembly of colloidal nanorods. *Nano Lett.* **5**, 2408–2413 (2005).
38. Wan, W., Sun, J., Su, J., Hovmöller, S. & Zou, X. Three-dimensional rotation electron diffraction: software RED for automated data collection and data processing. *J. Appl. Crystallogr.* **46**, 1863–1873 (2013).
39. Rietveld, H. A profile refinement method for nuclear and magnetic structures. *J. Appl. Crystallogr.* **2**, 65–71 (1969).
40. Ameri, T. et al. Fabrication, optical modeling, and color characterization of semitransparent bulk-heterojunction organic solar cells in an inverted structure. *Adv. Funct. Mater.* **20**, 1592–1598 (2010).
41. Matsui, M. Molecular dynamics study of $MgSiO_3$ perovskite. *Phys. Chem. Miner.* **16**, 234–238 (1988).
42. Berendsen, H., Grigera, J. & Straatsma, T. The missing term in effective pair potentials. *J. Phys. Chem.* **91**, 6269–6271 (1987).
43. de Araujo, A. S., Sonoda, M. T., Piro, O. E. & Castellano, E. E. Development of new Cd^{2+} and Pb^{2+} Lennard-Jones parameters for liquid simulations. *J. Phys. Chem. B* **111**, 2219–2224 (2007).
44. Mosconi, E., Azpiroz, J. M. & De Angelis, F. Ab initio molecular dynamics simulations of methylammonium lead iodide perovskite degradation by water. *Chem. Mater.* **27**, 4885–4892 (2015).
45. Plimpton, S. Fast parallel algorithms for short-range molecular dynamics. *J. Comput. Phys.* **117**, 1–19 (1995).
46. Vega, C., Abascal, J. & Nezbeda, I. Vapor–liquid equilibria from the triple point up to the critical point for the new generation of TIP4P-like models: TIP4P/Ew, TIP4P/2005, and TIP4P/ice. *J. Chem. Phys.* **125**, 034503 (2006).
47. Kumar, S., Rosenberg, J. M., Bouzida, D., Swendsen, R. H. & Kollman, P. A. The weighted histogram analysis method for free-energy calculations on biomolecules. I. The method. *J. Comput. Chem.* **13**, 1011–1021 (1992).
48. Chandler, D. Statistical mechanics of isomerization dynamics in liquids and the transition state approximation. *J. Chem. Phys.* **68**, 2959–2970 (1978).
49. Wang, F. & Landau, D. Efficient, multiple-range random walk algorithm to calculate the density of states. *Phys. Rev. Lett.* **86**, 2050–2053 (2001).
50. Weinan, E., Ren, W. & Vanden-Eijnden, E. Finite temperature string method for the study of rare events. *J. Phys. Chem. B* **109**, 6688–6693 (2005).